Sensor and Simulation Notes

Note 413

Multifunction Impulse Radiating Antennas: Theory and Experiment

Everett G. Farr
Farr Research, Inc.

Carl E. Baum and William D. Prather
Phillips Laboratory

November 1997

Abstract

A Multifunction IRA is an extension of a standard Impulse Radiating Antenna that has the additional flexibility of an adjustable beamwidth. This adjustability is implemented by defocusing the feed, in order to select between a narrow or broad beam. We provide here the theory of operation of the antenna, for both in-focus and out-of-focus situations. Furthermore, we built and tested a design with a 46 cm diameter. We found reasonable agreement of the experiment with theory, although some work remains to be done in refining the feed point.

I. Introduction

A reflector Impulse Radiating Antenna (IRA) consists of a parabolic reflector with a TEM feed. This class of antenna has a considerable body of literature associated with both its analysis and measurements [1-3]. One issue that has been raised concerning this type of antenna, however, is that the beamwidth is too narrow for many applications. In order to broaden the beam, we introduce the Multifunction IRA, or MIRA.

The principle behind the MIRA is quite simple. The feed point of an IRA is normally at the geometric focus of a parabolic reflector. In a MIRA, we defocus the feed arms slightly, by placing the feed point somewhat closer to the dish than its normal position at the focus of the reflector.

If one can add a mechanical control to the feed point location, then one can have a single antenna with a narrow or broad beam, as required. This results in a single antenna with very broad bandwidth and beamwidth control. Such an antenna may be useful in applications where a single antenna must serve multiple functions due to limited aperture space. In this note we develop the theory of such a device, and we describe the fabrication and testing of a prototype design.

The theory developed here is based on the quasistatic electric field in an aperture. In previous papers [2, 4-8], we have developed a number of techniques for calculating the radiated field when an aperture field is turned on uniformly, all at the same time. With a defocused aperture, however, the aperture is turned on gradually, beginning at the center. The theory is modified here that takes this gradual turnon into account. We provide here theoretical calculations of the radiated impulse in the H- and E-planes, for both focused and defocused aperture positions.

In addition, an experimental prototype was developed with an 46 cm (18 in) diameter reflector using four feed arms with an adjustable position. The position is controlled by a servo mechanism that is controlled by a personal computer.

By including computer control in the design, we allow a great deal of flexibility in system design. For example, one might use the MIRA as part of a radar system that can operate in either search mode, which requires a broad beamwidth, or tracking mode, which requires a narrow beamwidth. A block diagram of such an arrangement is shown in Figure 1.1. The controller would select which of two radar systems would be fed into the antenna. The controller would also set the antenna feed position, in order to control the beamwidth.

The field is measured using TEM sensors. These were developed based on an idea by C. J. Buchenauer[9] to enhance signal-to-noise ratio with very fast, low-voltage pulsers. These sensors are replicating sensors, not the derivative sensors that are perhaps more commonly used. We calibrate these sensors using two identical sensors.

Let us begin now with the theory that describes the MIRA. We begin with a review of the theory of a focused aperture.

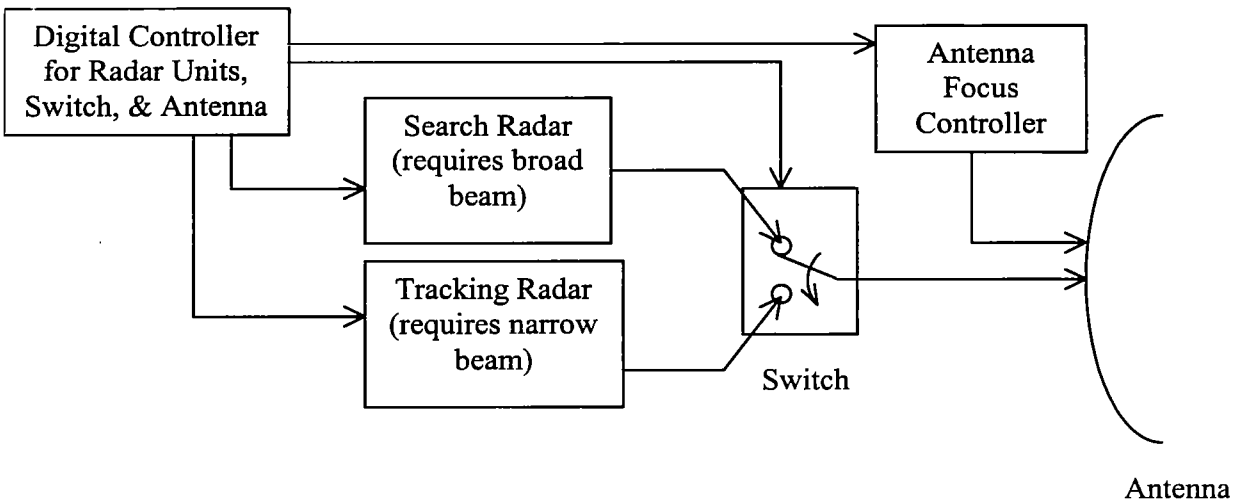

Figure 1.1. Control of the RF switch and antenna focus using a digital controller.

II. Review of Theory with Focused Aperture

To begin the calculation of the radiated field, we first review the theory for the focused aperture radiation. The theory for the defocused aperture will be a straightforward perturbation on the theory for the focused aperture. This section is mainly review, and draws heavily on [2, 8].

To evaluate the radiated fields, it is necessary to evaluate the fields in an aperture plane in front of the reflector. For a focused aperture, the fields are well known to be represented by the two-dimensional Laplace problems for the two-wire and four-wire apertures (Figure 2.1). The radiated field for our configuration is well approximated by the four-wire aperture. The fields in the four-wire aperture are described by a superposition of two two-wire apertures, as we will see later.

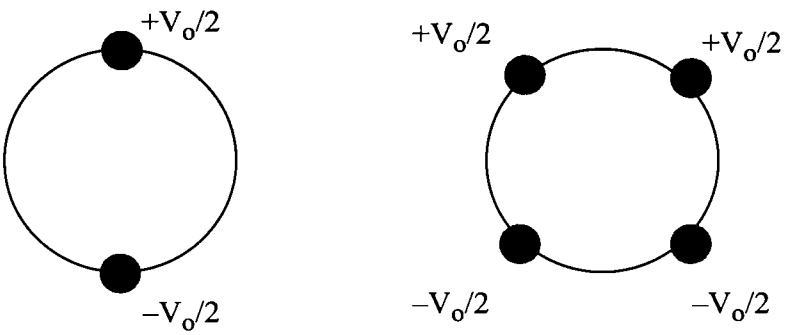

Figure 2.1. The apertures for a two-wire and four-wire configuration.

The first step is to find the fields in the aperture. To do so, we must first find the potential function that describes these fields. The potential function for the two-wire problem is well known,

$$w_2(\zeta) \;=\; 2j\,\mathrm{arccot}(\zeta/a) \;=\; \ln\!\left(\frac{\zeta/a - j}{\zeta/a + j}\right) \tag{2.1}$$

where the charge centers are located at (x=0, y/a = 1). Here, $\zeta = x + j\,y$ is the location in the Cartesian coordinate space. This potential function was plotted in [5, Figure 2], so there is no need to repeat it here. The complex potential for the four-wire case is just a sum of two two-wire potentials that have been shifted and resized, i.e.,

$$w_4(\zeta) \;=\; w_2\!\left((\zeta/a + \sqrt{2})/\sqrt{2}\right) \;+\; w_2\!\left((\zeta/a - \sqrt{2})/\sqrt{2}\right) \tag{2.2}$$

This function is complex, i.e., has both real and imaginary parts. Let us therefore set

$$u(\zeta) \;=\; \mathrm{Re}(w_4(\zeta)) \;,\qquad v(\zeta) \;=\; \mathrm{Im}(w_4(\zeta)) \tag{2.3}$$

We can plot contours of constant u and v, and these are shown in Figure 2.2 for the upper right quadrant. The conductors correspond to a contour of constant u.

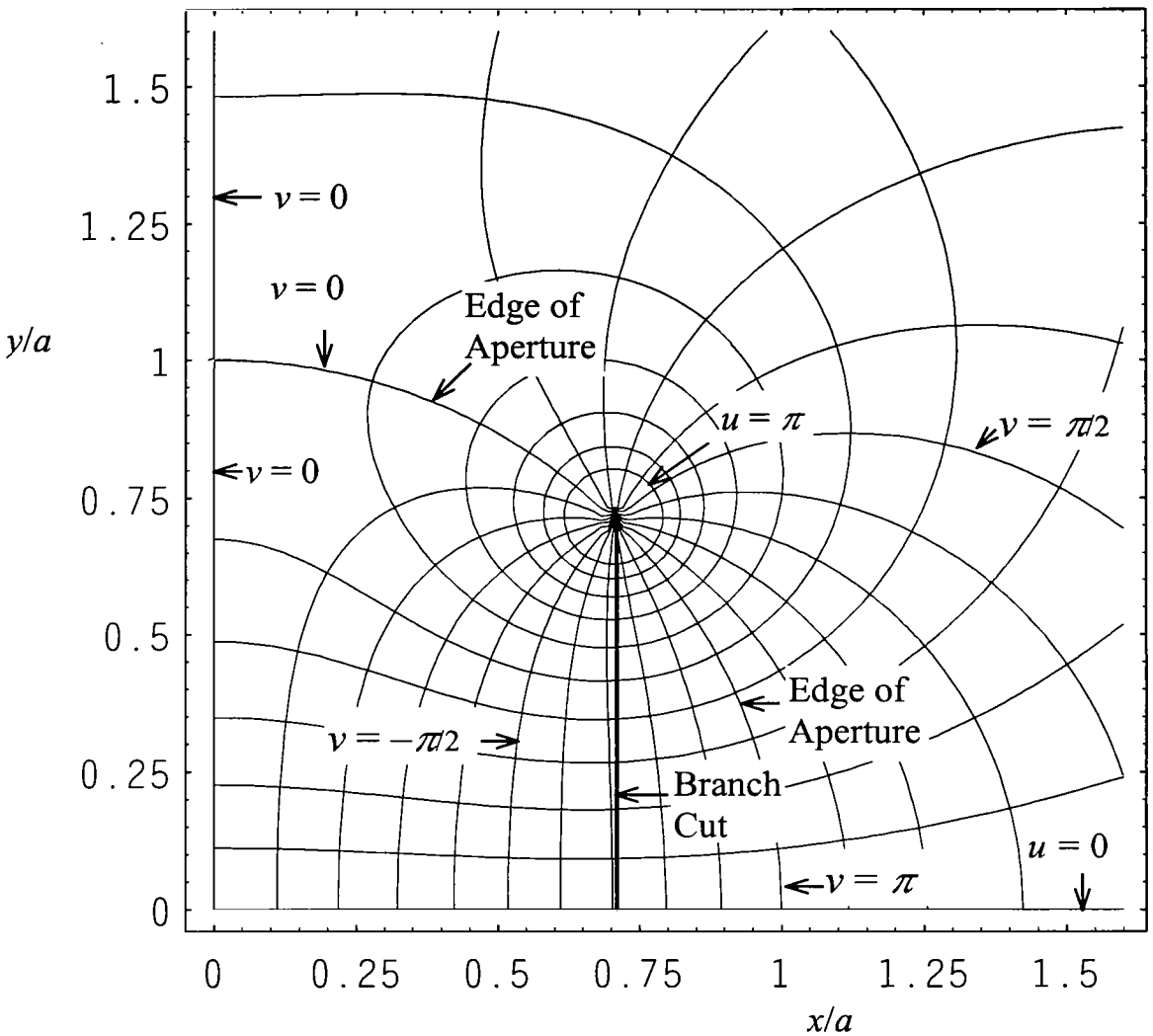

Figure 2.2. Contour map for $w_4(\zeta)$. Increments for both u and v are $\pi/10$.

To calculate the radiated field, we need the aperture fields and the normalized aperture potentials. First, we find the aperture field is

$$E_y(x,y) = \frac{-V_o}{\Delta u}\frac{\partial u(x,y)}{\partial y}, \qquad f_{g4} = \frac{\Delta u}{\Delta v} \tag{2.4}$$

where V_0 is the voltage difference between the top and bottom conductors. In addition, Δu is the difference in u between the two conductors, and Δv is the difference in v as one encircles one pair of positive (or negative) electrodes. Finally, the normalized aperture impedance is $f_{g4} = Z_{feed}/Z_o$, where Z_o is the impedance of free space. Note that f_{g4} is the normalized impedance for four arms and f_{g2} is the normalized impedance for two arms on opposite sides of a unit circle. Note also that for thin wire arms, $f_{g4} = f_{g2}/2$.

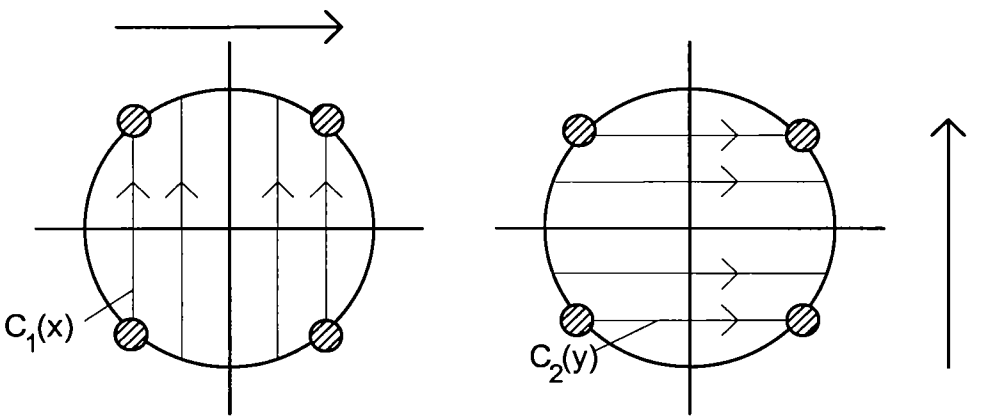

Figure 2.3. Locations of $C_1(x)$ and $C_2(y)$.

Next, we find the normalized potentials, which are integrals of electric field over linear paths in the aperture plane. The normalized potential for the H-plane calculation is

$$\Phi^{(h)}(x) = -\frac{1}{V_o}\int_{C_1(x)} E_y \, dy \tag{2.5}$$

where the contour $C_1(x)$ is a vertical line cut through the aperture plane, as shown in Figure 2.3. To simplify this, one substitutes (2.4) into (2.5), generating

$$\Phi^{(h)}(x) = \frac{1}{\Delta u}\int_{C_1(x)} \frac{\partial u}{\partial y}\, dy = \frac{2}{\Delta u}\, u\left(x, \sqrt{a^2 - x^2}\right) \tag{2.6}$$

We can now calculate $u(x,y)$ as the real part of the potential function given in (2.2). Note that the value of $u(x,y)$ is a maximum when it cuts through the conductors. At this point, the value of $u(x,y)$ is $u_o = \pi f_{g2} = 2\pi f_{g4}$, where f_{g4} is the normalized impedance for four arms (typically 200 Ω/□377 Ω). Note also that for values of x that cut through the conductors, the normalized

potential is unity. This normalized potential function is plotted in Figure 2.4, for a few different values of f_{g4}.

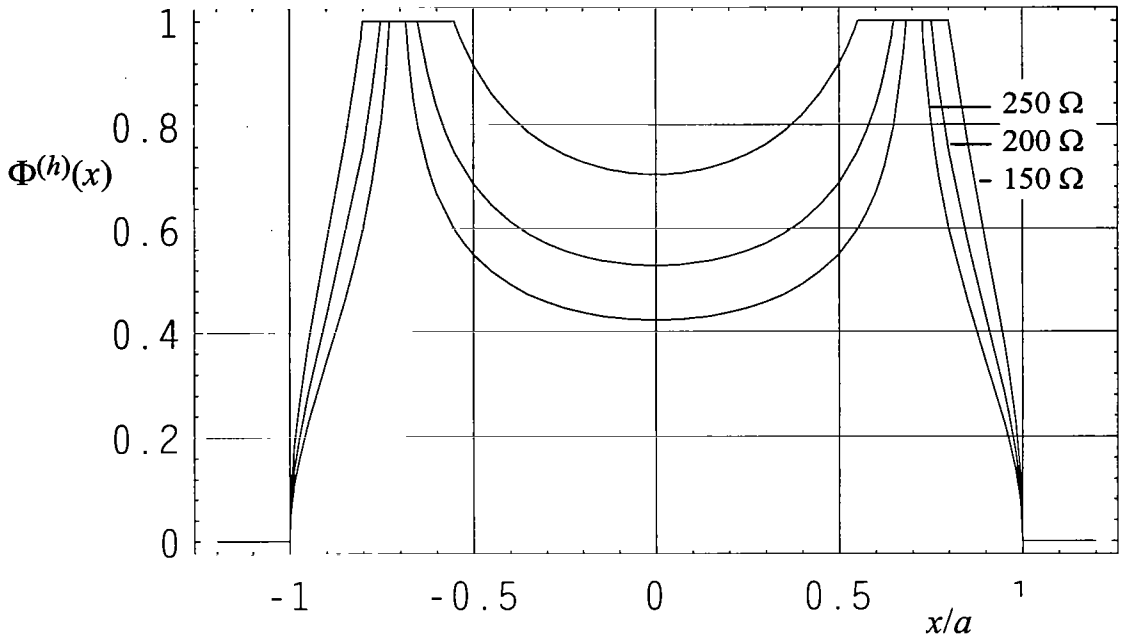

Figure 2.4. The normalized potential function of a 4-wire aperture, $\Phi^{(h)}(x)$, plotted for a few different four-wire feed impedances.

The normalized potential for the E-plane is expressed as

$$\Phi^{(e)}(y) = -\frac{1}{V_o}\int_{C_2(y)} E_y\, dx = \frac{1}{\Delta u}\int_{C_2(y)} \frac{\partial u}{\partial y}\, dx \tag{2.7}$$

where $C_2(y)$ is a horizontal linear cut through the aperture plane, as shown in Figure 2.5. To evaluate this, we require the Cauchy-Riemann relation for analytic functions,

$$\frac{\partial u}{\partial y} = -\frac{\partial v}{\partial x} \tag{2.8}$$

We can now recast the integral as

$$\Phi^{(e)}(y) = \frac{-2}{\Delta u}\left[v\left(\sqrt{a^2 - y^2}, y\right) - v(0, y)\right] \tag{2.9}$$

This is a particularly simple form, because the edges of the circular aperture are also lines of constant v. Thus, the normalized potential is evaluated analytically as

$$\Phi^{(e)}(y) = \begin{cases} 1/(2f_{g4}) & 0 \le |y|/a < 1/\sqrt{2} \\ 0 & \text{else} \end{cases} \tag{2.10}$$

We have plotted the normalized potentials for a few impedances in Figure 2.5. Note that our theory predicts an abrupt discontinuity in $\Phi^{(e)}(y)$ near the wires. In fact, there is actually a more smooth transition between the two values, but if the wire is thin, this is an excellent approximation.

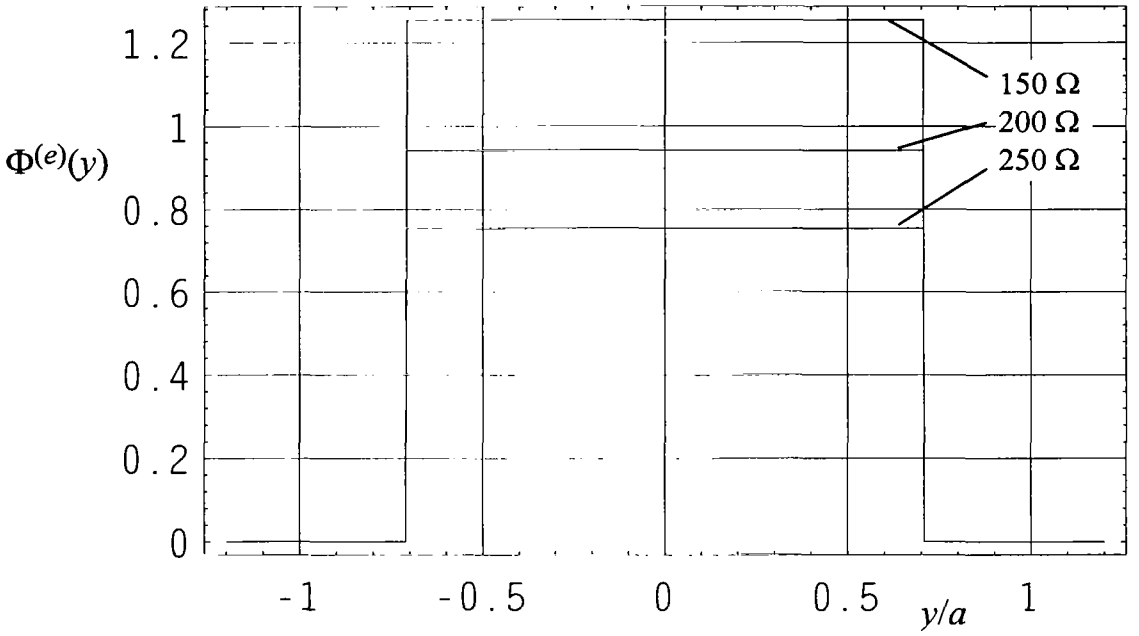

Figure 2.5. The normalized potential function of a 4-wire aperture, $\Phi^{(e)}(y)$, plotted for a few different four-wire feed impedances.

With the normalized potentials calculated, we can now calculate the radiated field as a function of angle off boresight in the H and E-planes. The aperture field is created by a step voltage of magnitude V_o across the aperture, so from [8] we find

$$\begin{aligned} \vec{E}_{step}{}^{(h)}(r,\theta,t) &= \vec{1}_y \frac{-V_o}{r} \frac{\cot(\theta)}{2\pi} \Phi^{(h)}\left(\frac{ct}{\sin(\theta)}\right) \\ \vec{E}_{step}{}^{(e)}(r,\theta,t) &= \pm \vec{1}_\theta \frac{-V_o}{r} \frac{1}{2\pi\sin(\theta)} \Phi^{(e)}\left(\frac{ct}{\sin(\theta)}\right) \end{aligned} \tag{2.11}$$

This completes the calculation of the step response radiation for a full 4-wire aperture, while it is still focused.

To find the response to a standard Gaussian pulse, we convolve the above step response with the derivative of the Gaussian. The Gaussian is described by

$$\frac{dV(t)}{dt} = \frac{V_o}{t_d} e^{-\pi(t/t_d)^2}, \qquad t_{FWHM} = 0.940\, t_d \tag{2.12}$$

$$V(t) = \int_{-\infty}^{t} \frac{dV(t')}{dt'} dt', \qquad t_{10-90} = 1.023\, t_d \tag{2.13}$$

where t_{FWHM} is the Full Width Half Max of dV/dt, and $t_{10\text{-}90}$ is the 10-90% risetime of $V(t)$. Note that we have expressed this conveniently in terms of the derivative risetime, which is inversely proportional to the radiated field for these types of antennas. The definition of the derivative risetime of a waveform is

$$t_d = \frac{\max\,(V(t))}{\max(dV(t)\,/\,dt)} \tag{2.14}$$

The radiated field is now calculated simply from

$$E(r,\theta,\phi,t) = \frac{1}{V_o}\frac{dV(t)}{dt} \circ E^{step}(r,\theta,\phi,t) \tag{2.15}$$

where $E^{step}(r,\theta,\phi,t)$ is the step response in the E- or H-plane, as calculated above.

Next we consider how to extend these results to a defocused aperture. We provide results for both focused and defocused cases in the section that follows.

III. Modification of Theory to Include Defocused Aperture

Having reviewed the theory for focused apertures, we now extend these results to a defocused aperture. To do so, we need to return to more general expressions for the field radiated from an aperture. Thus, we have from [10, eqn 2.7]

$$\begin{aligned} \vec{E}(\vec{r},s) &= \frac{1}{2\pi r}\iint_{S_a} \gamma\left[\vec{1}_z \times \vec{E}_t(x',y',s)\times \vec{1}_R\right] e^{-\gamma R}\, dA \\ &= \frac{s}{2\pi r c}\iint_{S_a}\left[\vec{1}_z \times \vec{E}_t(x',y',s)\times \vec{1}_R\right] e^{-s R/c}\, dA \end{aligned} \tag{3.1}$$

where primed coordinates refer to the aperture plane, and unprimed coordinates refer to the observation point. Furthermore, $\vec{E}_t(x',y',s)$ is the tangential aperture field in the aperture plane, and S_a is the aperture surface. The aperture plane is the x'-y' plane (at z'=0). Note that the above equation differs from [10 eqn 2.7] by retaining only the far-field ($1/r$) term, and by substituting $\gamma = s/c$. The expressions for r and R are

$$\begin{aligned} r &= \sqrt{x^2+y^2+z^2} \\ R &= \sqrt{(x-x')^2+(y-y')^2+(z-z')^2} \end{aligned} \tag{3.2}$$

We will shortly specialize the above expressions for the radiated field to the H- and E-planes, but before we do so, we first wish to describe the form of the aperture field.

The form of the tangential aperture electric field is

$$E_y(t) = -\frac{V_o}{\Delta u}\frac{\partial u(x',y')}{\partial y'} W(t) \tag{3.3}$$

where $u(x', y')$ is the potential function described previously in (2.2)-(2.3). Furthermore, $W(t)$ is a window function that takes into account the gradual illumination of the aperture. This is illustrated in Figure 3.1. Thus, $W(t)$ is a window that is circular in shape, with a radius described by $\Psi_a(t')$. We assume that the curved phase front first touches the center of the aperture at t'= 0, so at $\Psi_a(t'=0) = 0$. Furthermore, the instant where the aperture is first completely filled is denoted by t'_{max}, so $\Psi_a(t'_{max}) = \Psi_{a,max}$.

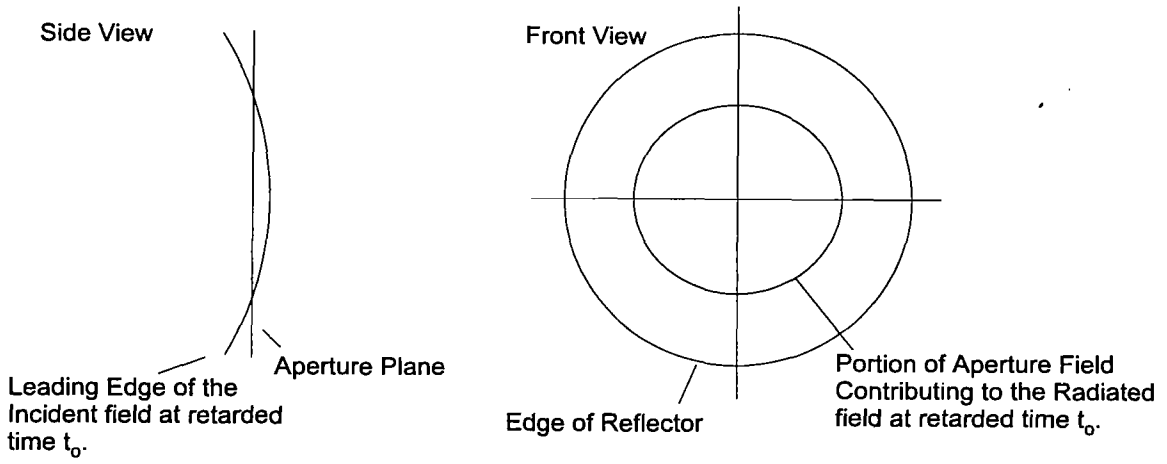

Figure 3.1. Illustration of how a defocused aperture is filled gradually by the incident field (left). The portion of the aperture plane contributing to the aperture field is shown on the right.

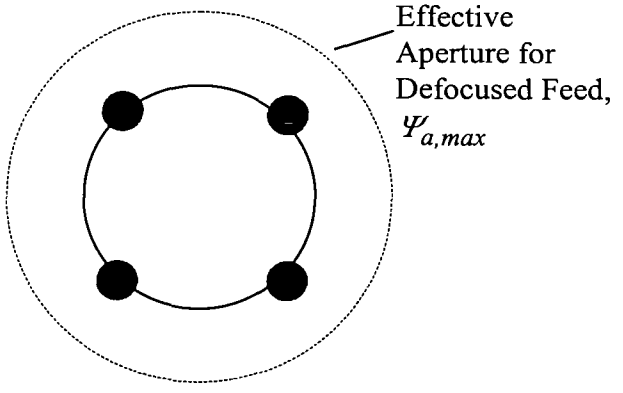

Figure 3.2. The extent of the effective aperture, when a rigid feed arm assembly is pushed closer to the reflector.

Note that some care must be taken when determining the position where above potential function is evaluated. The position in the aperture plane, (x',y'), must be mapped onto a position in a flat virtual plane (x_v, y_v), using stereographic projections. If we describe a position on the aperture in the polar (cylindrical) coordinates, (Ψ',ϕ'), it is necessary to map the position on the aperture onto a virtual plane, described by (Ψ_v,ϕ_v), shown in Figure 3.2. To do so, we use geometric optics to trace the ray that arrives at (ϕ', Ψ'). This ray has an origin at the feed point, and it points in the direction $(\theta_{inc}, \phi_{inc})$. Due to symmetry, we have

$$\phi' = \phi_{inc} = \phi_v \tag{3.4}$$

so we have only left to find Ψ_v.

To find Ψ_v, we first find θ_{inc} by geometric optics and ray tracing. In other words, we find the angle of departure of the ray that begins at the feed point and arrives at (Ψ', ϕ'). Thus,

having found θ_{inc}, we need only find a relationship between θ_{inc} and Ψ_v. The geometry is shown in Figure 3.3.

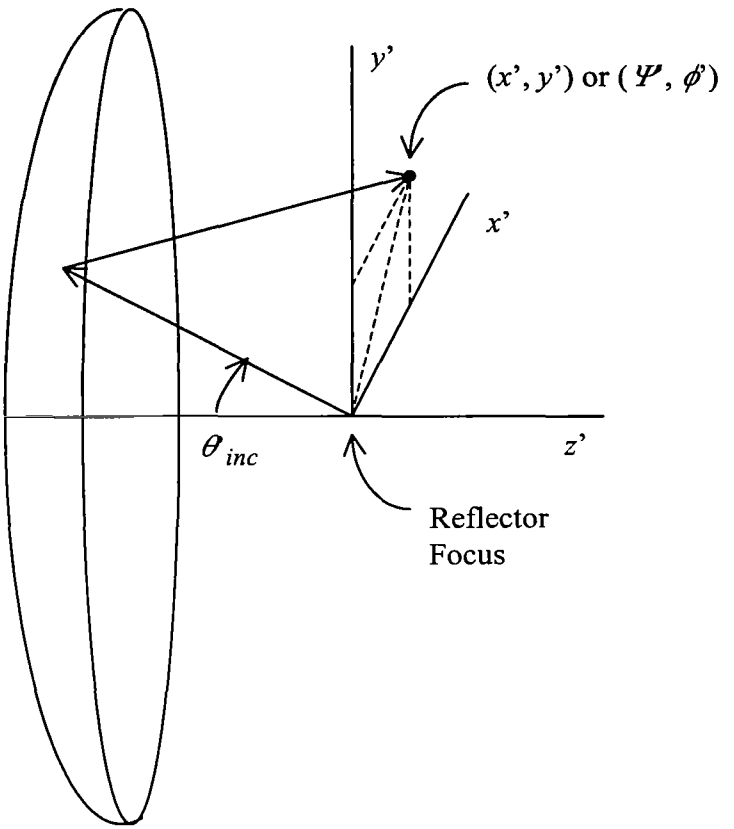

Figure 3.3. The ray trace from the focus to a point in the aperture plane.

To complete the process of calculating Ψ_v, we compare the stereographic projection of (Ψ', ϕ') to that of the charge center of the feed arms. We know the charge center of the feed arms projects onto the unit circle in the virtual plane, so $\Psi_{v,o} = 1$. Now by taking a ratio of stereographic projections,

$$\Psi = 2F \tan(\theta/2) \tag{3.5}$$

we obtain

$$\begin{aligned} \Psi_v &= \Psi_{v,o} \frac{\tan(\theta_{inc}/2)}{\tan(\theta_{inc,o}/2)} \\ \phi_v &= \phi' \end{aligned} \tag{3.6}$$

The only remaining unknown in this equation is the incident angle of the charge center. This is found from the F/D ratio of the reflector, f_d, so

$$\theta_{inc,o} = \arctan\left[\frac{1}{2f_d - 1/(8f_d)}\right] \tag{3.7}$$

and we now have both Ψ_v,and ϕ_v., From these two, we can calculate (x_v,y_v), so we have completed our procedure for mapping (x',y') into (x_v,y_v).

Having described the aperture fields, we now restrict the expression for the radiated field, (3.1), to the H-plane and E-plane. We begin with the H-plane.

A. H-Plane Calculation

In the H-plane the dominant component of the radiated field is the y-component. Furthermore, only the y-component of the aperture field contributes to the y-component of the radiated field due to symmetry. Thus, after restricting the tangential field to the y-component, we have

$$\begin{aligned} \vec{1}_z \times \tilde{\vec{E}}_t(x',y',s) \times \vec{1}_R &= \vec{1}_y \, \tilde{E}_y(x',y',s)\cos(\theta) \\ R &\cong r - x'\cos(\theta) \end{aligned} \tag{3.8}$$

Substituting the above relationships into (3.1), we have, in both frequency and time domains,

$$\begin{aligned} \tilde{E}_y^{(h)}(\theta,s) &= \frac{s\cos(\theta)}{2\pi r c} \iint_{S_a} \tilde{E}_y(x',y',s)\, e^{-(s/c)(r-x'\cos(\theta)} \, dA \\ E_y^{(h)}(\theta,t) &= \frac{\cos(\theta)}{2\pi r c} \frac{d}{dt} \iint_{S_a} \tilde{E}_y(x',y',t-(r-x'\cos(\theta))/c) \, dA \end{aligned} \tag{3.9}$$

where the superscript (h) indicates that the expression is specific to the H-plane. For simplicity, we convert to retarded time, $t' = t - r/c$, so

$$E_y^{(h)}(\theta,t') = \frac{\cos(\theta)}{2\pi r c} \frac{d}{dt} \int dx' \int dy' \, E_y(x',y',t+(x'/c)\cos(\theta)) \tag{3.10}$$

We now need to account for the time-varying nature of S_a. As stated previously, the aperture expands as a function of time, with a radius $\Psi_a(t')$. Thus, the limits of integration over the aperture change with time. Let us define

$$\Phi^{(h)}(x',t') = -\frac{1}{V_o}\int_{-y_{max}(x't')}^{y_{max}(x',t')} dy'\ E_y(x',y')$$

$$y_{max}(x',t') = \begin{cases} 0 & t'<0 \\ \sqrt{\Psi_a{}^2(t') - x'^2} & 0 \le t' \le t_{max} \\ \Psi_{a,max} & t'>0 \end{cases} \tag{3.11}$$

This is closely analogous to equation (2.5), with the exception that there is an additional time dependence. The integration is carried out along a straight line of constant x', with limits that are determined by $W(t)$, the window function that describes the effective aperture radius as a function of t'. If we now combine the above expression with (3.3), we have

$$\Phi^{(h)}(x',t') = \frac{2}{\Delta u}\ u(x', y_{max}(x',t')) \tag{3.12}$$

By combing equations (3.10-3.12) we have

$$\boxed{E_{y,step}{}^{(h)}(\theta,t') = -\frac{V_o}{2\pi r c}\cos(\theta)\ \frac{d}{dt}\int dx'\,\Phi^{(h)}(x', t'-(x'/c)\sin(\theta))} \tag{3.13}$$

This is now in a form that can be implemented numerically. Note that one can tabulate $\Phi^{(h)}(x',t')$ in order to avoid repetitive calculations. Then, $E_{y,step}{}^{(h)}(\theta,t')$ is calculated by a one-dimensional integral. Thus, we have successfully converted a double integral over the aperture to a single integral, which should be more numerically efficient. Note also that when calculating $u(x',y')$ it is necessary to calculate it into the virtual plane, as shown in equation (3.6).

B. E-Plane Calculation

Next, we calculate the radiated field in the E-plane. The derivation is very similar to that in the H-plane. The dominant component is the θ component , and once again, we need only calculate the y-component of the aperture field due to symmetry. This leads to

$$\vec{1}_z \times \tilde{\vec{E}}_t(x',y',s) \times \vec{1}_R = \vec{1}_y\ \tilde{E}_y(x',y',s)$$
$$R \cong r - y'\cos(\theta) \tag{3.14}$$

Substituting the above relationships into (3.1), we have, in both frequency and time domains,

$$\begin{aligned}
\tilde{E}_\theta^{(e)}(\theta,s) &= \frac{s}{2\pi r c} \iint_{S_a} \tilde{E}_y(x',y',s)\, e^{-(s/c)(r-x'\cos(\theta)}\, dA \\
E_\theta^{(e)}(\theta,t) &= \frac{1}{2\pi r c}\, \frac{d}{dt} \iint_{S_a} \tilde{E}_y(x',y',t-(r-y'\cos(\theta))/c)\, dA
\end{aligned} \tag{3.15}$$

where the superscript (e) indicates that the expression is specific to the E-plane. As before, we convert to retarded time, $t' = t - r/c$, so

$$E_\theta^{(e)}(\theta,t') = \frac{1}{2\pi r c}\, \frac{d}{dt} \int dy' \int dx'\, E_y(x',y',t+(y'/c)\cos(\theta)) \tag{3.16}$$

We now need to account for the time-varying nature of S_a. As stated previously, the aperture expands as a function of time, with a radius $\Psi_a(t')$. Thus, the limits of integration over the aperture change with time. Let us define

$$\begin{aligned}
\Phi^{(e)}(y',t') &= -\frac{1}{V_o} \int_{-x_{max}(y',t')}^{x_{max}(y',t')} dy'\; E_y(x',y') \\
x_{max}(y',t') &= \begin{cases} 0 & t' < 0 \\ \sqrt{\Psi_a{}^2(t') - y'^2} & 0 \le t' \le t_{max} \\ \Psi_{a,max} & t' > 0 \end{cases}
\end{aligned} \tag{3.17}$$

This is closely analogous to equation (2.7), with the exception that there is an additional time dependence. The integration is carried out along a straight line of constant y', with limits that are determined by $W(t)$, the window function that describes the effective aperture radius as a function of t'. Note that one must take care in calculating $\Phi^{(e)}(x',t')$, due to the branch cut in the contour map. If we now combine the above with (3.3), we have

$$\begin{aligned}
\Phi^{(e)}(y',t') &= \frac{1}{\Delta u} \int_{-x_{max}(t')}^{x_{max}(t')} \frac{\partial u}{\partial y}\, dx \;=\; -\frac{1}{\Delta u} \int_{-x_{max}(t')}^{x_{max}(t')} \frac{\partial v}{\partial x}\, dx \\
&= -\frac{2}{\Delta u} \left[v(x'_{max}(y',t'),y') - v(0,y') \right]
\end{aligned} \tag{3.18}$$

where we have used the relationship $\partial u / \partial x = -\partial v / \partial y$. Care must be used in the application of the above formula for the difference of two v's if a branch cut is crossed. In that case, a term of 2π must be subtracted from the difference in square brackets above. If we combine the above three equations, we have

$$\boxed{E_{\theta,step}{}^{(e)}(\theta,t') = -\frac{V_o}{2\pi r c}\, \frac{d}{dt} \int dy'\, \Phi^{(e)}(y', t' - (y'/c)\sin(\theta))} \tag{3.19}$$

This is now in a form that can be implemented numerically. Once again, we have converted a double integral over the aperture into a single integral, which is faster to calculate. Note that the position where the potential function $v(x',y')$ is calculated must be mapped onto the virtual plane as described in equation (3.6).

Having calculated the step response in both the H-and E-planes, we now convolve with a Gaussian, as shown previously in (2.15), to obtain the far field with a finite-risetime step response.

As an example, we calculated the radiated field in the H- and E-planes for a 46 cm (18 in) diameter reflector MIRA with $F/D = 0.5$, a risetime $t_d = 50$ ps and a feed impedance of 200 Ω.

Let us define now a ratio that describes the focal position. Let F be the focus of the reflector, and F_2 be the distance from the feed point to the reflector. Then we define a ratio

$$f_f = \frac{F_2}{F} \tag{3.20}$$

When the feed is located at the focus, $f_f = 1$. In our MIRA, we can adjust the focal point from $f_f = 0.7$ to $f_f = 1.0$. In the data we present here, $f_f = 0.7$, 0.85, and 1.0. The definition of f_f is shown in Figure 3.4.

The radiated field for $f_f = 1.0$ (feed at the focus) is shown in Figure 3.5. Both the H-plane and E-plane cuts are shown, for values off-boresight of 0, 7.5, and 15 degrees. We can clearly see that the field goes down as we proceed off-boresight in either plane. Furthermore, the radiated field for $f_f = 0.85$ and 0.7 are shown in Figures 3.6 and 3.7, respectively. From these plots, we can see that the peak field on boresight is reduced as we progressively defocus the antenna.

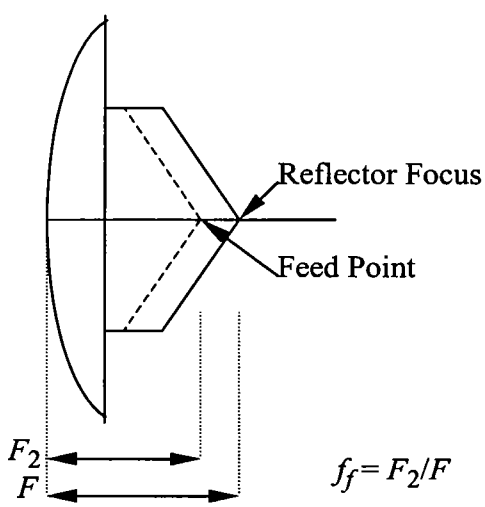

Figure 3.4. Definition of f_f.

Next, we need to define a beamwidth for this antenna, in order to compactly describe the data. We define the half field beamwidth (HFBW) as the angle between the two locations in a pattern cut where the field is down by half from the peak. Since we ran data at discreet angles off-boresight, the best we can do is estimate beamwidths. Furthermore, note that these beamwidths are specific to the particular choice of risetime, i.e., $t_d = 50$ ps. Finally, note that we estimate full beamwidths, not half beamwidths from boresight.

The HFBWs are provided in Table 3.1. From the data it is clear that the MIRA's beam broadens from about 8° when in focus, to about 36° when at the maximum defocus of $f_f = 0.7$. This is true in both the H- and E-planes. This is precisely the behavior we were hoping to find in this antenna.

Having demonstrated the relevant properties in theory, we now turn to experiment to verify the result.

Table 3.1. MIRA Half Field Beam Widths

	Half Field Beam Width (HFBW)	
$f_f = F_2/F$	H-Plane	E-Plane
1.00	8°	10°
0.85	15°	15°
0.70	36°	36°

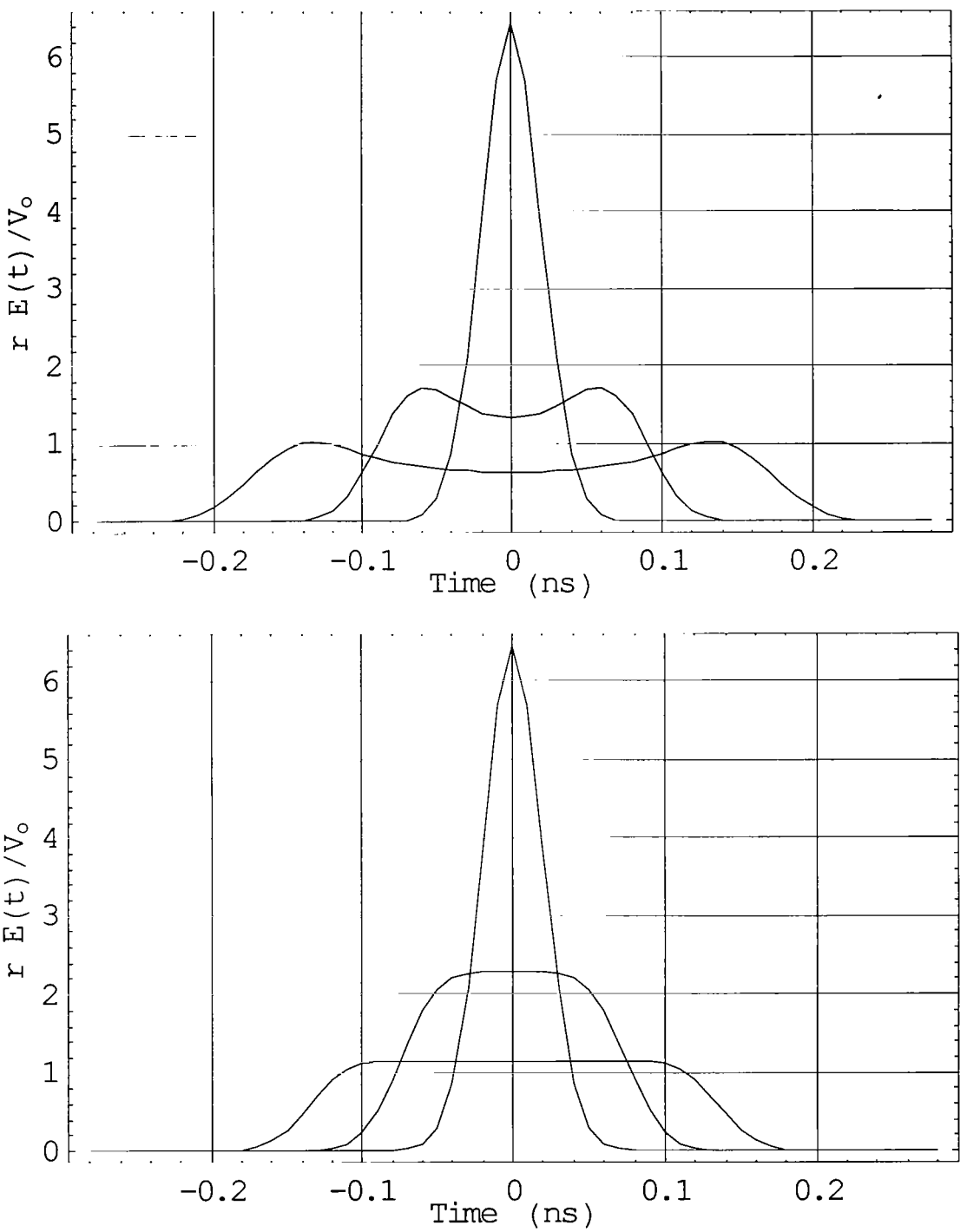

Figure 3.5. MIRA radiated field, f_f = 1.0 (in focus), H-plane (top) and E-plane (bottom), at angles of 0, 7.5, and 15 degrees off-boresight.

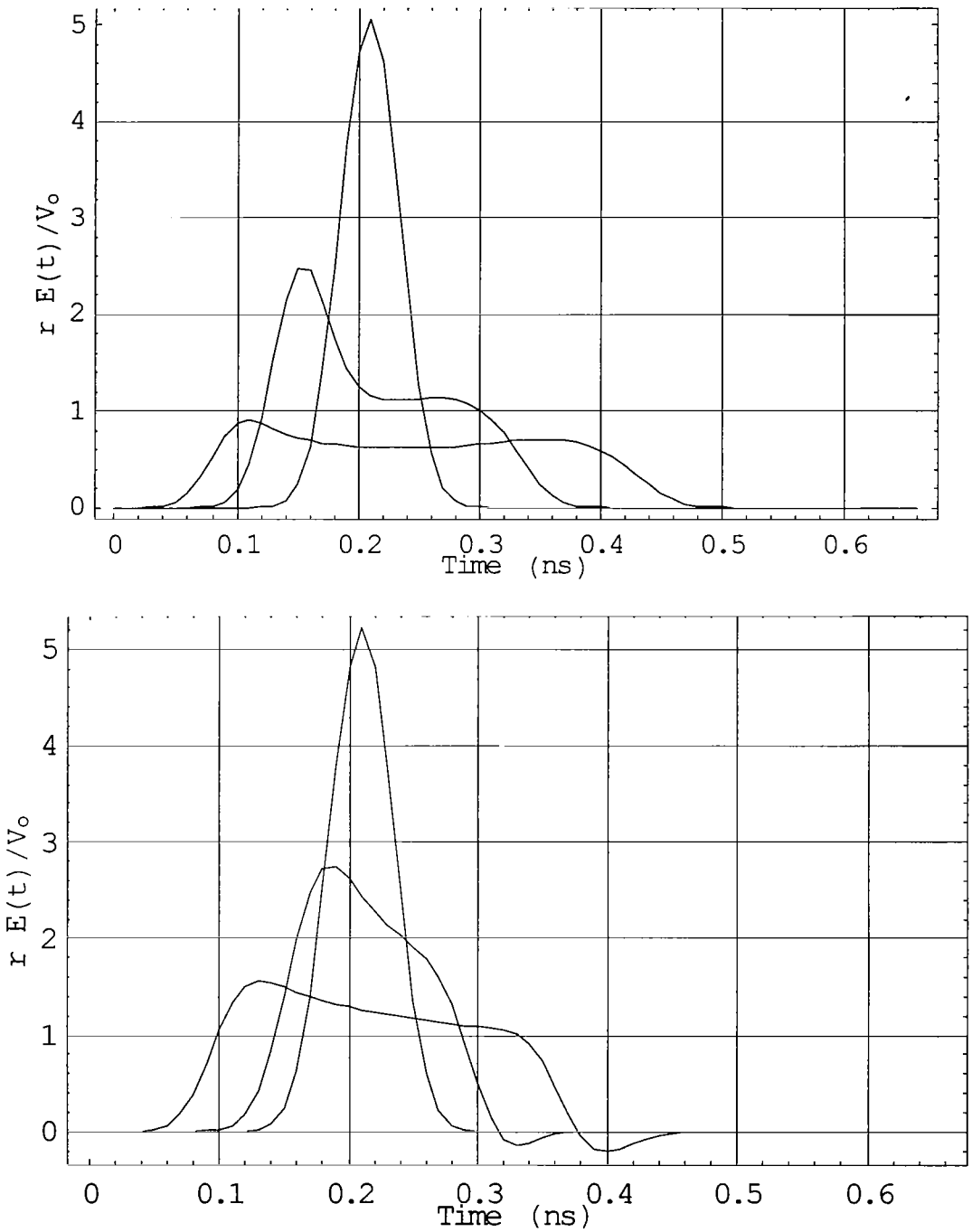

Figure 3.6. MIRA radiated field, f_f = 0.85, H-plane (top) and E-plane (bottom), at angles of 0, 7.5, and 15 degrees off-boresight.

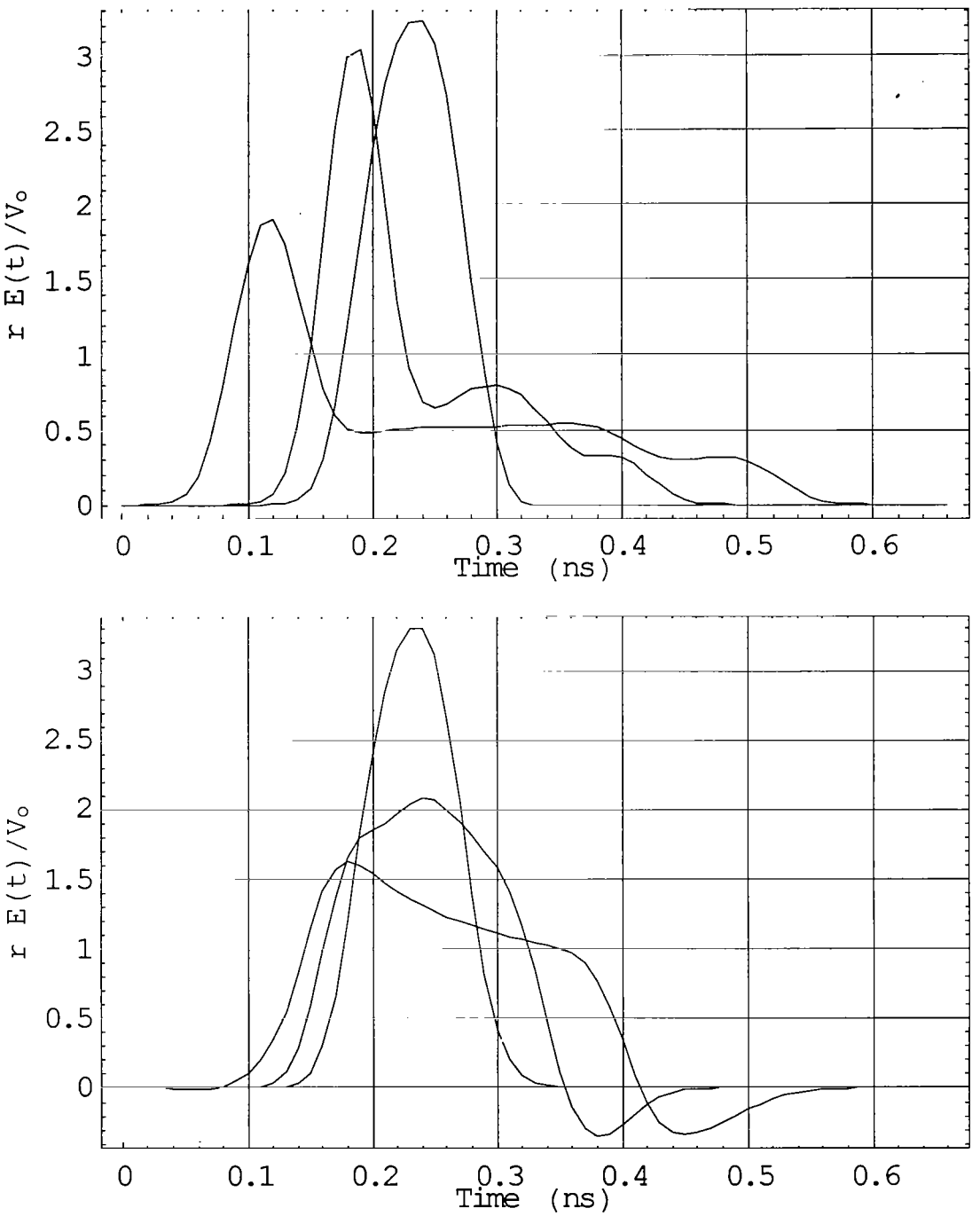

Figure 3.7. MIRA radiated field, $f_f = 0.7$, H-plane (top) and E-plane (bottom), at angles of 0, 7.5, and 15 degrees off-boresight.

IV. Experimental Validation

In order to demonstrate the MIRA experimentally, we built a model with a diameter of 46 cm (18 in), with adjustable feed arms.

A diagram of the configuration as built is shown in Figures 4.1 and 4.2. It includes a solid 18-inch diameter parabolic reflector that slides along a set of four fixed feed arms. A servo motor controls the position of the reflector with respect to the feed, and a laptop computer communicates with the servo controller using a serial port.

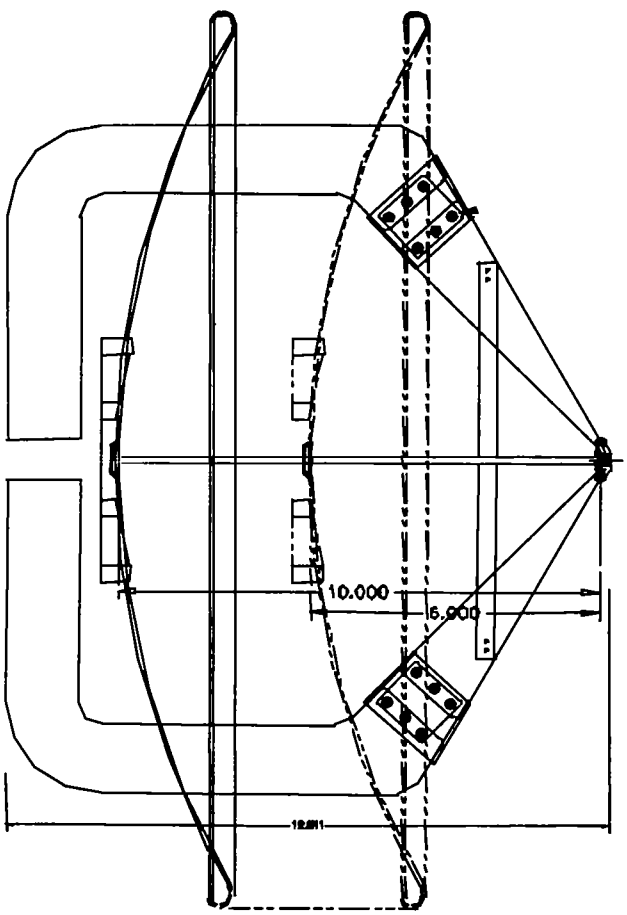

Figure 4.1. The Multifunction IRA, side view.

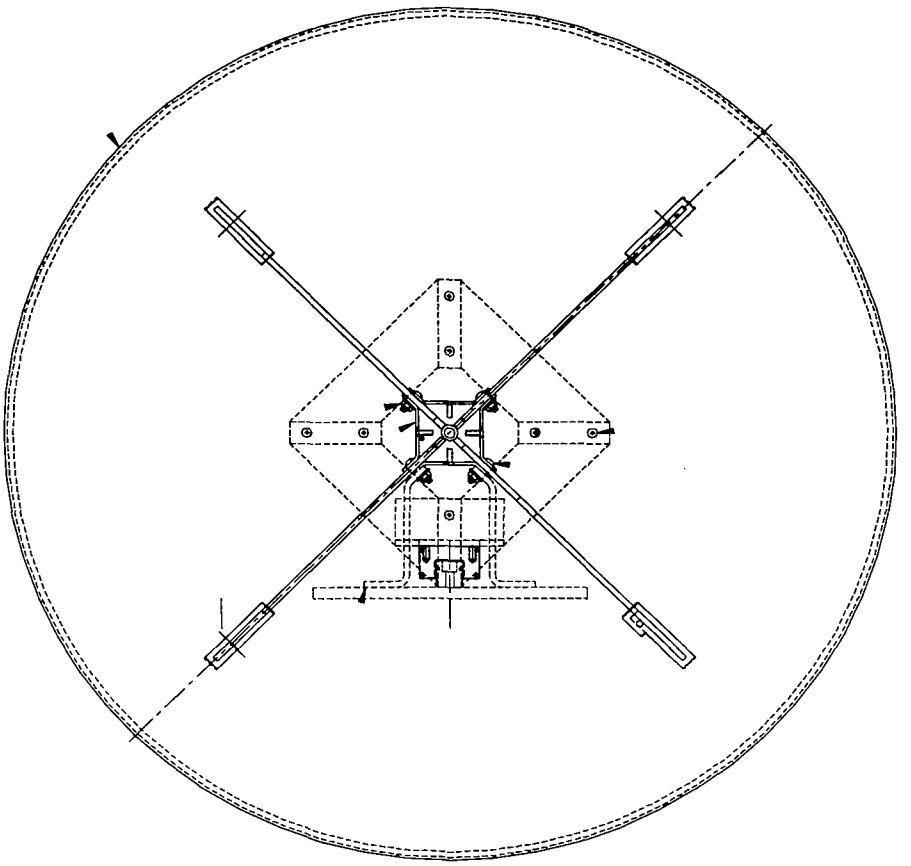

Figure 4.2. The Multifunction IRA, front view.

The reflector was made of solid aluminum, and the feed arms were tin-coated copper. The F/D ratio was 0.5, and the feed impedance was 190 Ω. The antenna was fed with the so-called "splitter balun," of the type first described by C. Baum in [11]. This type of balun normally uses two 100 Ω cables connected in parallel at the feed end and in series at the antenna apex. However, it was difficult to find 0.141-inch diameter semi-rigid cable with 100 Ω impedance, so we had to use 95 Ω cables. We believe the error is small enough for our purposes. Note also that the feed arms were designed to form a 190 Ω transmission line, which is consistent with the two 95 Ω lengths of feed cable.

It was necessary to develop sensors that could be used to measure the radiated field. Standard derivative-type sensors have a very low sensitivity, so any measurements we made with our four-volt source would have been very noisy. Thus, we decided to develop a replicating sensor, which would replicate the incident electric field from the boresight direction. The design was essentially a half TEM horn mounted against a truncated ground plane (Figure 4.3). The ground plane was solid aluminum, and the conical plate was tin-plated copper. The impedance of the horn was 50 Ω, in order to avoid a mismatch to the 50 Ω electronics. The length of the horn was 45 cm. The top plate was supported with polystyrene foam for support.

The experimental test configuration for the antenna measurements is shown in Figure 4.4. In includes a Picosecond Pulse Labs 4015C step generator, which drives a TEM sensor. On the receive end, the Multifunction IRA receives the signal, which is then sampled by the SD24 sampling head and the Tektronix 11801B Digital Sampling Oscilloscope (DSO). Data is then downloaded to a computer for processing by way of a GPIB connection.

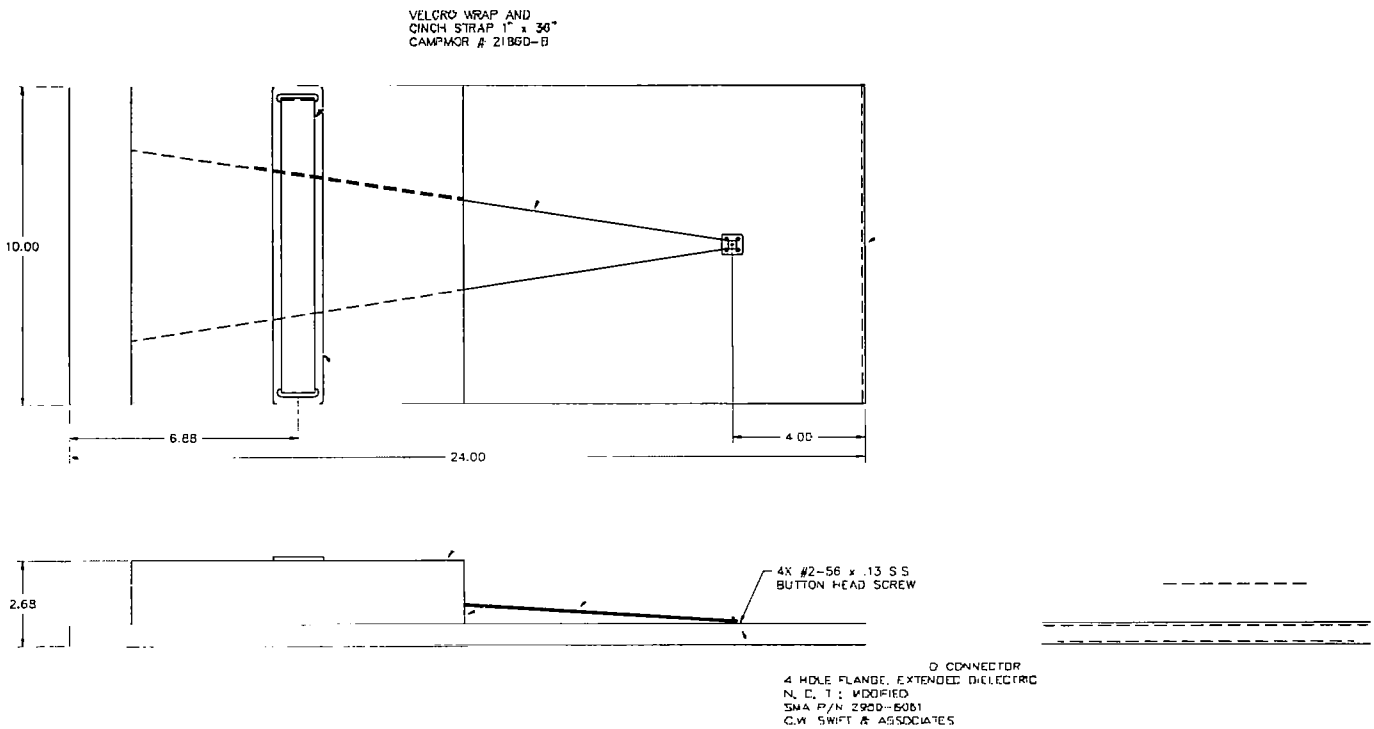

Figure 4.3. TEM Sensor. (Dimensions are inches.)

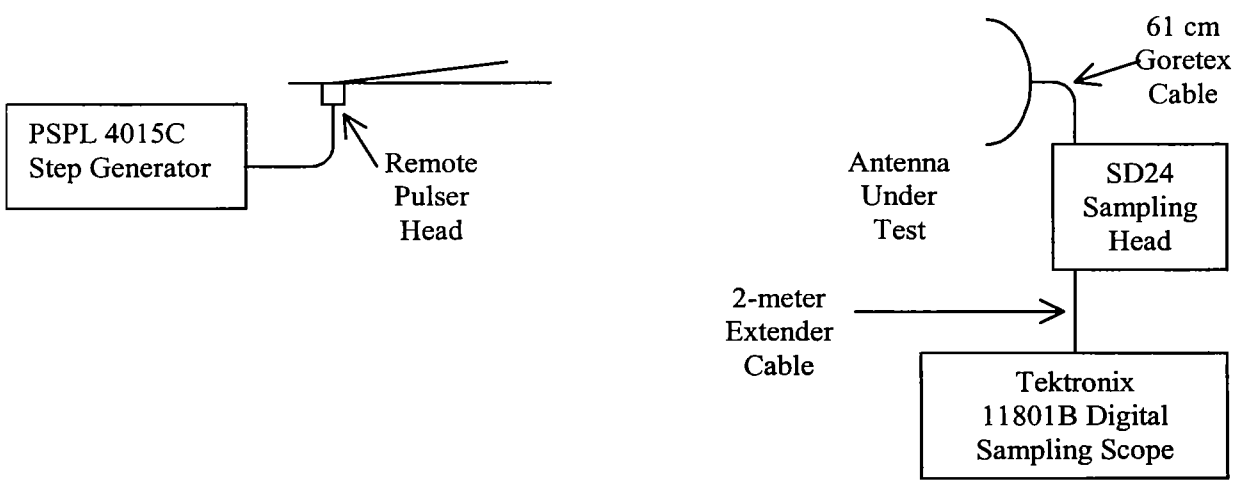

Figure 4.4.Experimental test setup

Before measuring the response of the MIRA, it is necessary to calibrate the TEM sensor. To do so, we measured the response of two identical TEM sensors, and then backed out the impulse response, using

$$V_{rec}(t) = \frac{1}{2\pi r c f_{g,tem}} h_{tem}(t) \circ h_{tem}(t) \circ \frac{dV_{src}(t)}{dt} \tag{4.1}$$

where $h_{tem}(t)$ is the impulse response of the TEM sensor, $V_{src}(t)$ is the source voltage, and $V_{rec}(t)$ is the raw received voltage. Furthermore, $f_{g,tem}$ is the normalized impedance of the TEM sensor, c is the speed of light in free space, and the " $\circ$ " symbol indicates convolution. The only unknown in the above equation is $h_{tem}(t)$, and we solve for that using the techniques described in [12, Section III]. Note that we are using r to be the distance between the front edges of the two TEM sensors. There is some ambiguity here, since the sensors are large enough that there is some field variation over the length of the sensors.

The source voltage is shown in Figure 4.5. It is a relatively clean step function with risetime of 28 ps. Next we took a measurement with the two identical TEM sensors, measured 3.35 meters apart. The raw data for this measurement is shown in Figure 4.6. It consists of a relatively clean impulse, with t_{FWHM} = 50 ps. Next, the data is processed to extract $h_{tem}(t)$, and the result is shown in Figure 4.7 in the frequency domain, and Figure 4.8 in the time domain. The result in the time domain is an almost-clean impulse with t_{FWHM} = 33 ps.

Next, we provide the integral of $h_{tem}(t)$, shown in Figure 4.9. The degree to which this integral is a clean step function is a measure of whether we can use the TEM sensor data raw, without correction. The integral is a step with some sag for the first 1.5 ns. (Note that some sag is expected, due to the characteristics of all TEM horns.) The jump in this integral gives us the effective height of the sensor. That is, assuming the voltage out of the sensor is (approximately) proportional to the incident field, the jump in this integral gives us the proportionality factor, or effective height, h_{eff}. We find that the magnitude of this jump is about 17 mm. Note that the plate is 31 mm above the ground plane in the aperture, so the measured h_{eff} is a little more than half of the physical aperture height. For an ideal geometry, we expect h_{eff} to be exactly half the physical aperture height [13], but the lip on the front edge of the ground plane would tend to increase the number slightly. Thus, our measurement of h_{eff} is consistent with theory.

Finally, we provide the TDR of the TEM sensor. The data is shown in Figure 4.10. A flat TDR indicates a good match to the 50 Ω input. We find the TDR is flat to within a few percent.

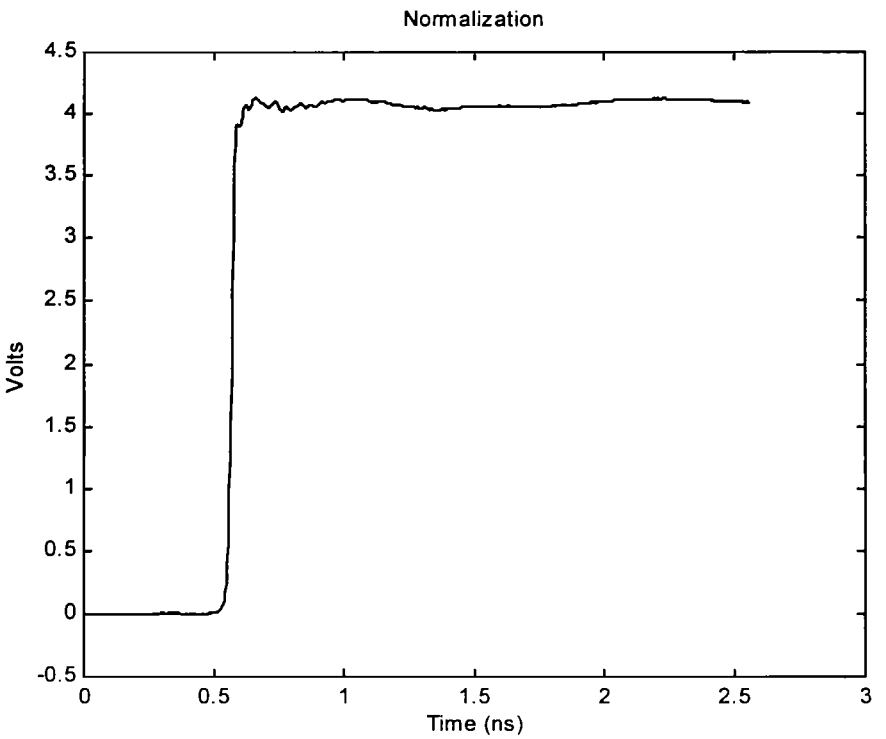

Figure 4.5. Source waveform

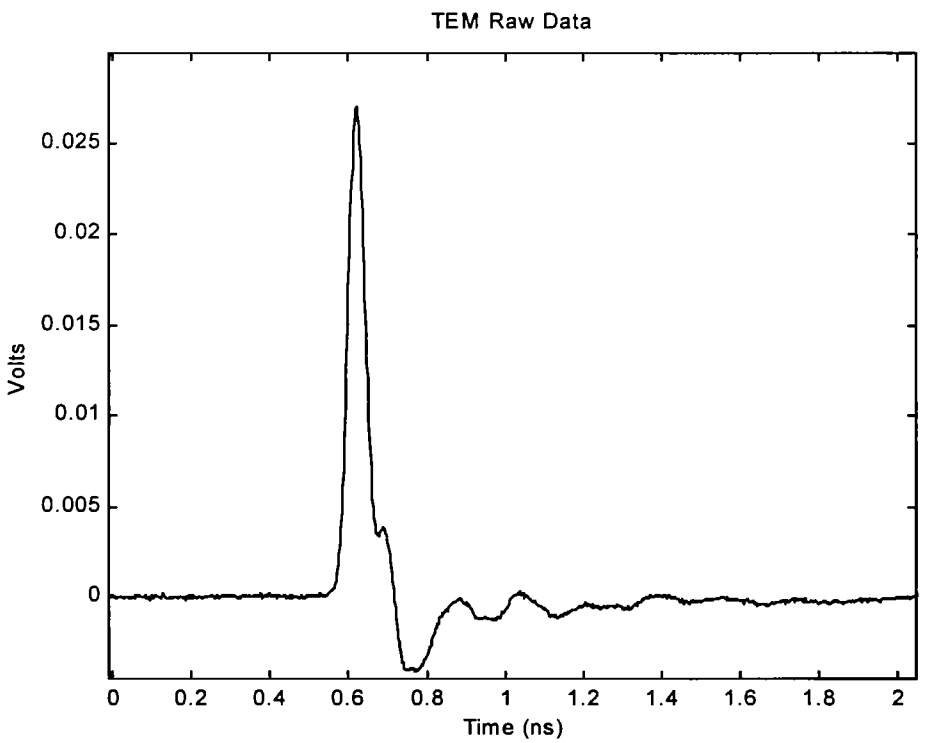

Figure 4.6. Raw received waveform for TEM sensor calibration.

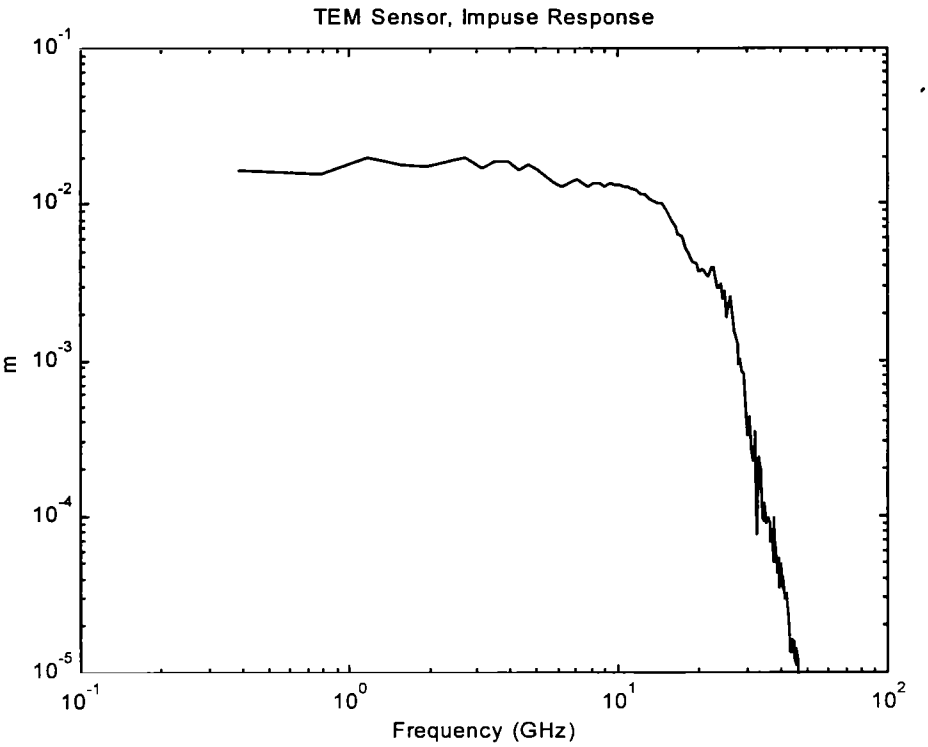

Figure 4.7. TEM sensor impulse response, $h_{tem}(\omega)$, in the frequency domain.

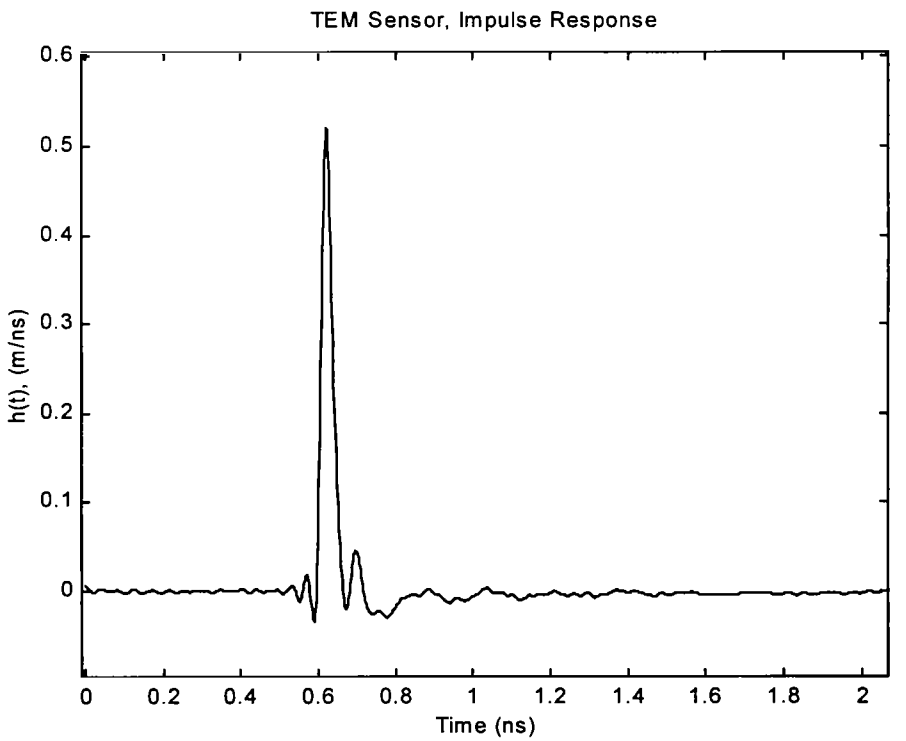

Figure 4.8. TEM sensor impulse response, $h_{tem}(t)$, in the time domain.

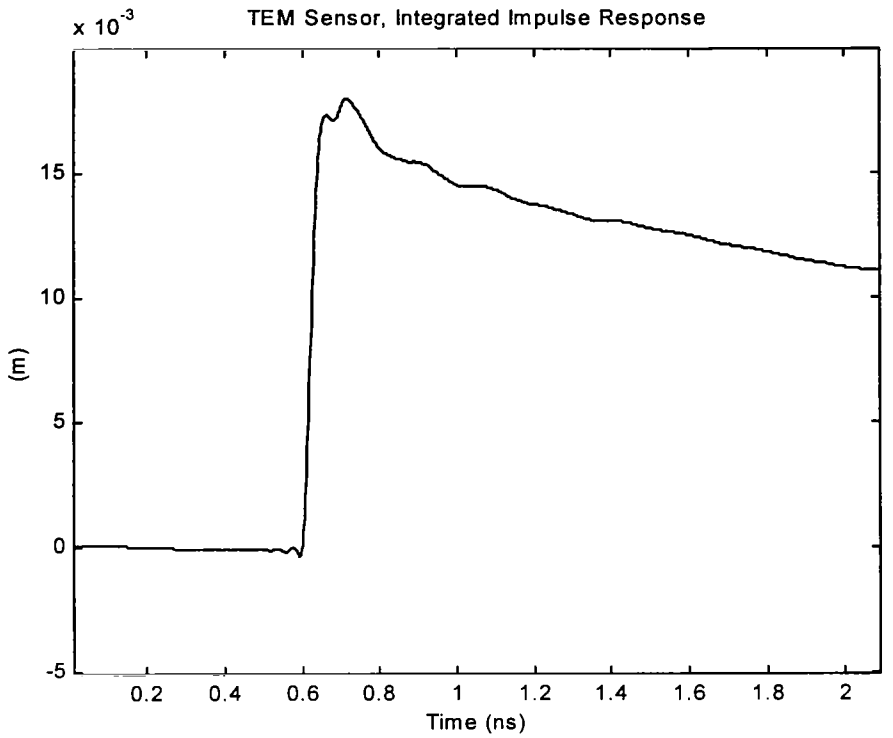

Figure 4.9. Integral of the TEM sensor impulse response.

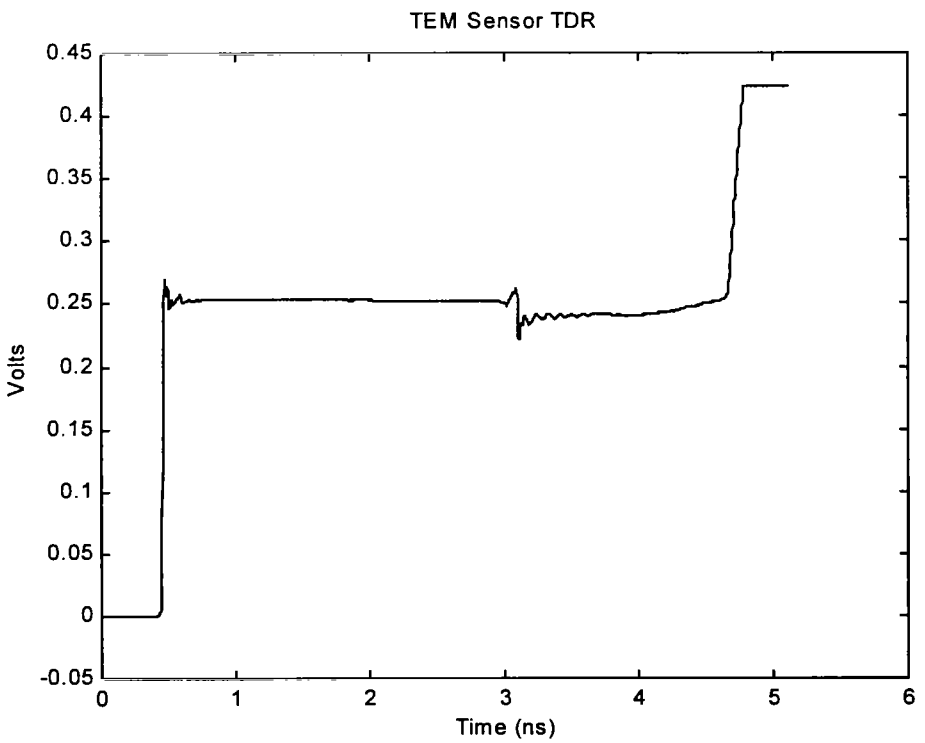

Figure 4.10. TDR of the TEM sensor.

Having characterized the sensor, we next measured the response of the MIRA. The data was taken at a distance of 3.25 meters, using the TEM sensor to detect the signal. The boresight response for the MIRA is shown in Figure 4.11, in both the time and frequency domains. It displays the classic time-domain waveform of a low-level prepulse, followed by a sharp impulse, with Full Width Half Max of 60 ps. Note that this is raw received voltage. The impulse has a shoulder formation, or a second impulse of a smaller magnitude. This can also be seen in the frequency response, which shows a dip near 5 GHz. This feature is due to some features that improved mechanical stability. Because of these features, the antenna has been made very sturdy, at some expense to electrical performance. It will be necessary to trade off mechanical and electrical properties in later designs.

Next, we consider the antenna pattern as a function of angle off-boresight, and as a function of focus position. Using the definition of focal position provided earlier in equation (3.20), we made our measurements at focal positions of $f_f = 1.0$, 0.85, and 0.7. Furthermore, data were taken at positions of 0°, 7.5°, and 15° off boresight in the H-plane. The raw data for all nine waveforms is shown in Figure 4.11. Once again, we see the peak field is reduced as we go off-boresight, and as we become more defocused.

With the above data, we can estimate the beamwidths of this antenna for various focus settings in the H-plane. We use here the definition of Half Field Beam Width (HFBW) as described in Section III. These beam widths are tabulated in Table 4.1, and they are compared to the theoretical values calculated earlier in Section III. We find general agreement with the trends in the experimental and theoretical data, however, there are some differences between them. The most significant difference is the estimate of the HFBW when $f_f = 1.0$ (in focus), for which our theory and measurement differ by a factor of almost two. This difference can probably be attributed to the difficulty of estimating the beamwidth with a small number of time waveforms. In addition, the sensor may be too close to the antenna under test to be a true far-field measurement. This would also tend to broaden the pattern.

Table 4.1. MIRA Half Field Beam Widths

	H-Plane Half Field Beam Width (HFBW)	
$f_f = F_2/F$	Theory (Section III)	Measurement
1.00	8°	15°
0.85	15°	24°
0.70	36°	30°

Next, we wish to compare the measured peak voltages to the theoretical peak radiated fields provided in Section III. To do so, we normalize our measured voltages to a factor of ($V_o \times h_{eff} / r$), where V_o = 4 V is the source voltage, r = 3.25 m is the antenna-sensor distance, and h_{eff} = 0.017 m is the approximate effective height of the sensor as measured earlier in this section. This provides a normalization factor of 21 mV. If we divide our measured voltages by this normalization factor, we are in the same unitless dimensions of $r \times E / V$ as the normalized field data in Section III. As an example, when the antenna is in focus, (f_f = 1.0), we get a theoretical value of rE/V_o = 6.2 from Figure 3.4. We compare this to Figure 4.12, where the peak impulse (above the prepulse baseline) is 42 mV. If we divide this by the normalization factor of 21 mV, we get a peak normalized radiated field of 2.0, which is 32% of the predicted value. This can be explained by the double-bump in the apex waveform, and the possibility that the measurements were taken somewhat in the near field.

Finally, we provide the TDR of the MIRA in Figure 4.12, using the 0.25-Volt source built into the SD-24 sampling head. We want to see a smooth match to 50 Ohms, but there are some reflections at the feed point. We expect to smooth this out in later designs.

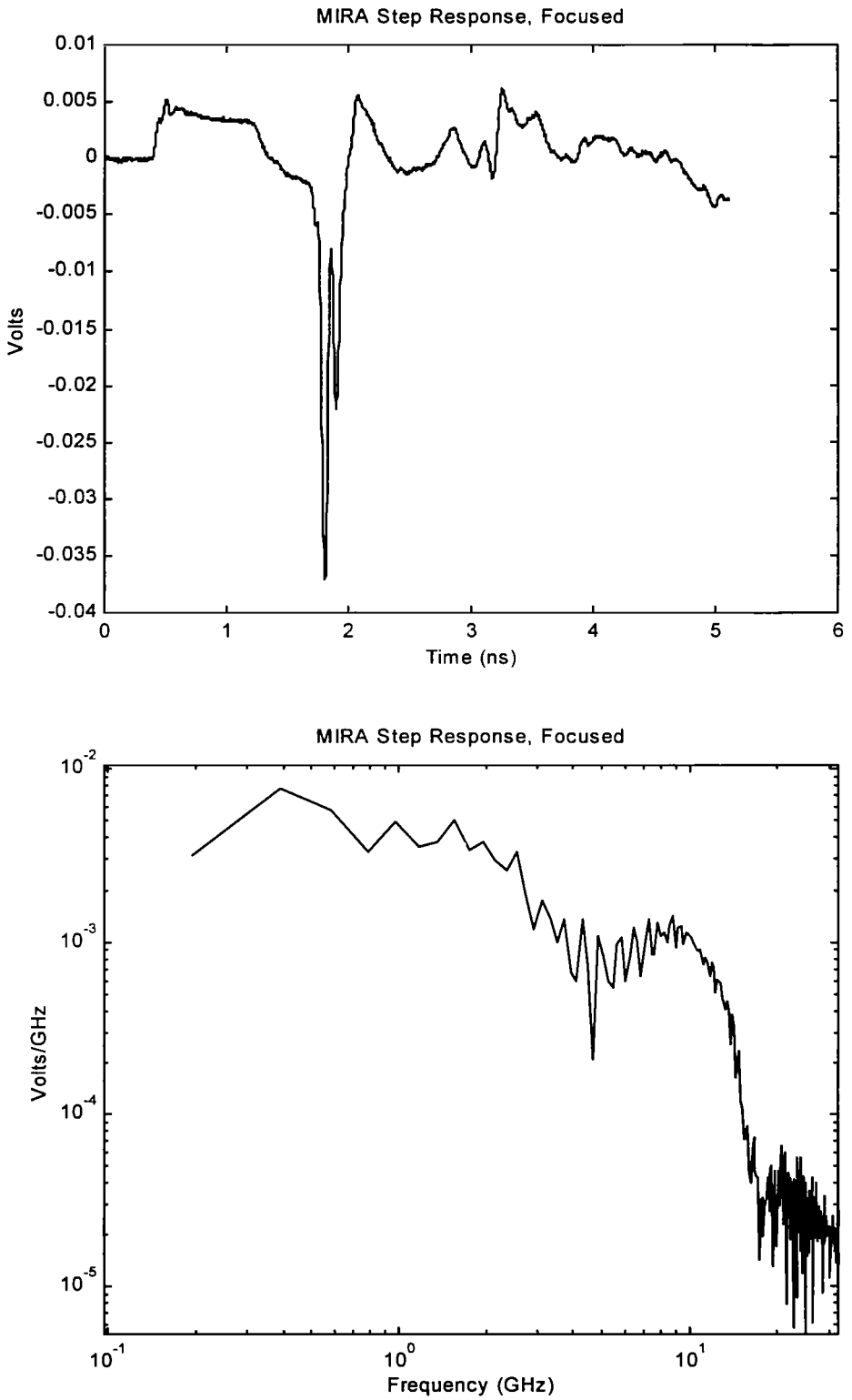

Figure 4.11. Boresight step response of the Multifunction IRA, in the time domain (top) and frequency domain (bottom).

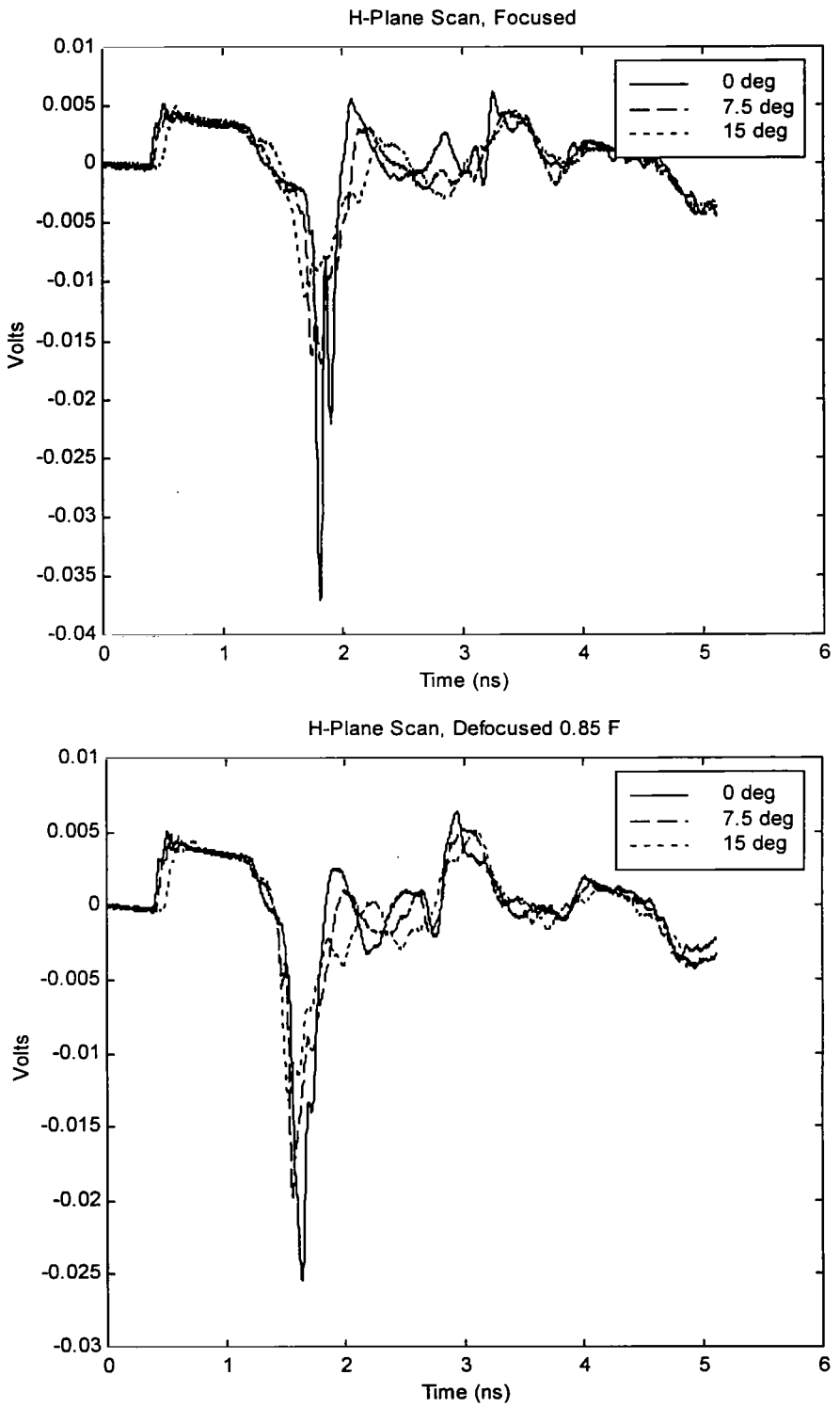

Figure 4.12. Antenna response for MIRA with $f_f = 1.0$ (top), and $f_f = 0.85$ (bottom). Antenna responses are for 0, 7.5, and 15 degrees off boresight in the H-plane. The results for $f_f = 0.70$ are on the next page.

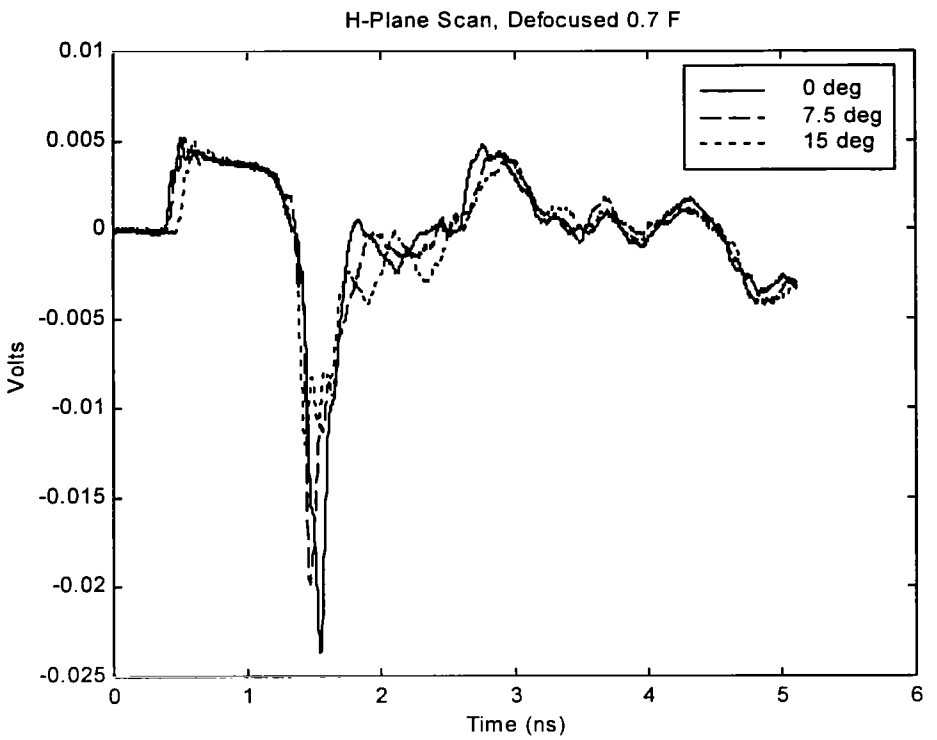

Figure 4.12 (cont'd). Antenna response for MIRA with $f_f = 0.70$. Antenna responses are for 0, 7.5, and 15 degrees off boresight in the H-plane.

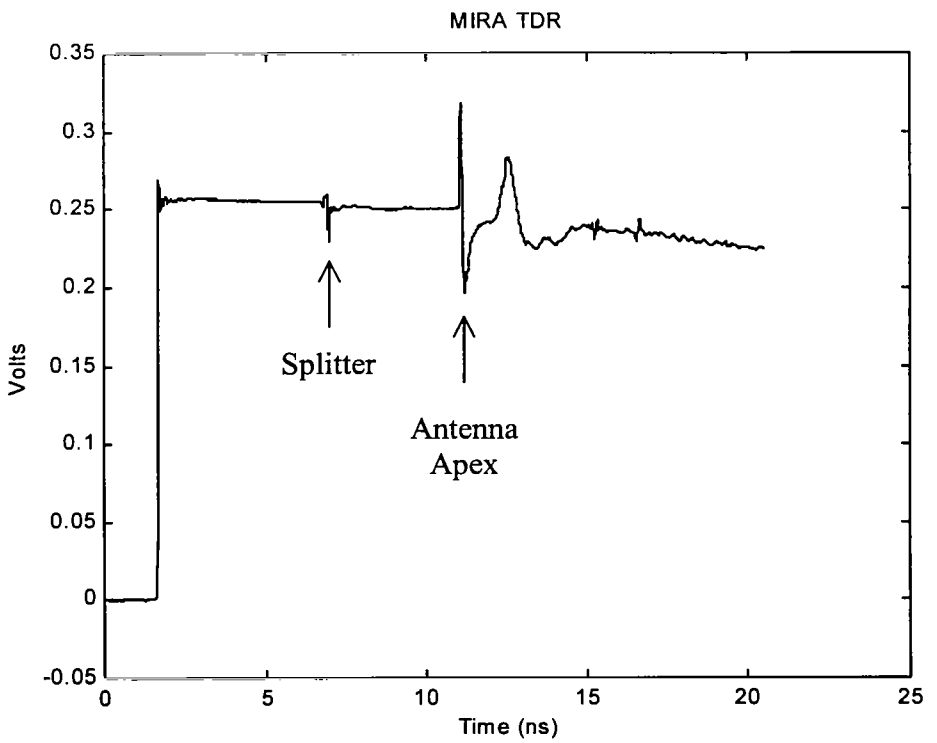

Figure 4.13. TDR of the MIRA.

V. Conclusions

We have provided here the theory that describes the MIRA, and we have built and tested a model with 46 cm diameter. Satisfactory agreement was obtained between theory and measurements, although refinements will be necessary. These refinements include a better impedance match at the MIRA apex. It will also be necessary to take more data at other greater distances, in order to verify that it is taken in the far field.

References

1. C. E. Baum and E. G. Farr , Impulse Radiating Antennas, pp. 139-148 in H. L. Bertoni *et al* (eds.), *Ultra-Wideband, Short-Pulse Electromagnetics*, New York, Plenum Press, 1993.

2. E. G. Farr, C. E. Baum, and C. J. Buchenauer, Impulse Radiating Antennas, Part II, pp. 159-170 in L. Carin and L. B. Felsen (eds.), *Ultra-Wideband, Short-Pulse Electromagnetics 2*, New York, Plenum Press, 1995.

3. E. G. Farr, C. E. Baum, and C. J. Buchenauer, Impulse Radiating Antennas, Part III, pp. 43-56 in C. E. Baum *et al* (eds.), *Ultra-Wideband, Short-Pulse Electromagnetics 3*, New York, Plenum Press, 1997.

4. C. E. Baum, Radiation of Impulse-Like Transient Fields, Sensor and Simulation Note 321, November 25, 1989.

5. E. G. Farr and C. E. Baum, The Radiation Pattern of Reflector Impulse Radiating Antennas: Early-Time Response, Sensor and Simulation Note 358, June, 1993.

6. E. G. Farr, Off-Boresight Field of a Lens IRA, Sensor and Simulation Note 370, October 1994.

7. E. G. Farr and G. D. Sower, Design Principles of Half Impulse Radiating Antennas, Sensor and Simulation Note 390, December 1995.

8. E. G. Farr and C. A. Frost, Development of a Reflector IRA and a Solid Dielectric Lens IRA, Part I: Design, Predictions and Construction, Sensor and Simulation Note 396, April 1996.

9. C. J. Buchenauer and R. Marek, Antennas and Field Sensors for Time Domain Measurements: An Experimental Investigation, pp. 197-208 in L. Carin and L. B. Felsen (eds.) *Ultra-Wideband, Short-Pulse Electromagnetics 2*, New York, Plenum Press, 1995.

10. C. E. Baum, Focused Aperture Antennas, Sensor and Simulation Note 306, May 1987.

11, C. E. Baum, Configurations of TEM Feed for an IRA, Sensor and Simulation Note 327, April 1991.

12. E. G. Farr and C. A. Frost, Compact Ultra Short Pulse Fuzing Antenna Design and Measurements, Sensor and Simulation Note 380, June 1995.

13. C. E. Baum, Aperture Efficiencies for IRAs, Sensor and Simulation Note 328, June 1991.